Advances in Bending Flat Plate Shape Memory Alloy Actuation Modeling: Prediction of Actuation Behavior

Michael Halvorson*, Jonathan Coleman**, Logan Williams**, Bryan Hardaker**, Frank Brown**, Noah Cargile**, Hayden Patteson** and Eric Bradshaw**

Abstract

A predictive model for the actuation of bent, flat nitinol plates was created with thermomechanical, kinematic, and constitutive relations; bent nitinol plates representing hinge actuators for deployable solar arrays with large moments of inertia were fabricated, shape trained, and actuation tested to evaluate performance against model behavior predictions. Model results were highly sensitive to nitinol residual stress and critical stress constant, parameters that may differ for fabricated nitinol specimens even within the same specimen batch, but model results were in excellent agreement with test results overall. The model assumed nitinol transitioned from fully detwinned martensite to austenite, and neither full detwinning nor a lack of nitinol rhombohedral or glass transition phases could be accurately determined by differential scanning calorimetry in the utilized specimens. Therefore, despite comparison of predictive model results to empirical test results, the model is considered to be neither verified nor validated; limited consideration is provided for test results. The predictive model is characterized fully.

Introduction

Shape Memory Alloys (SMA) such as nitinol are among the highest energy density actuators [1-2], with nitinol displaying controllable properties during use. Significant research has been performed to characterize the actuation of linear nitinol systems [3-6], but accurate prediction of flat plate SMA actuation under bending conditions has been limited in both scope and application [7-9]. A framework was developed to predict the bending actuation of flat plate nitinol SMA under non-standard geometric conditions yielding rise time of the actuating system. The framework includes a heat treatment procedure to prepare the material for actuation, a geometry-specific heat transfer model including phase change, conduction, convection, and radiation, a Finite Element Analysis (FEA) of mechanical bending stresses, and a kinematic model to simulate actuation across the bend region. This model is an improvement on the single-node bend framework presented in Halvorson et al. [10]. A single flat plate actuating to a deployed angle of 135° is shown in Figure 1, and the full test apparatus with three flat plates is shown in Figure 2.

Three flat nitinol plates were fabricated by water jet cutting and mounted to the test apparatus shown in Figure 2. Each SMA strip was 15-mm wide by 80-mm long by 0.5-mm thick with the bend line centering at 27-mm length. SMA material outside the minimum bending radius was for Patch Heater (PH) or bracket mounting purposes only. The plates were heat treated and shape trained to ensure desired deployment geometry. A HK6900 polyimide flexible PH from Minco was layered above and below with electrically insulating Kapton® film; the PH and Kapton assembly was tie-mounted to the SMA strip using heat-resistant Kevlar® thread. Both Kapton and Kevlar are registered products of DuPont; neither are shown on Figure 2. The SMA bend line was directly to the left of the PH in Figure 2; the PH was placed directly after the bend line to avoid stretching or compressing the PH during SMA acutation. The SMA was mounted via fasteners to a stationary base plate and rotating plate with controllable moment of inertia; the rotating plate was manually rotated into the non-deployed U-shape prior to actuation. Upon powering the PHs to heat the

* University of Alabama in Huntsville, Huntsville, AL; mch0043@uah.edu

** Auburn University, Auburn, AL

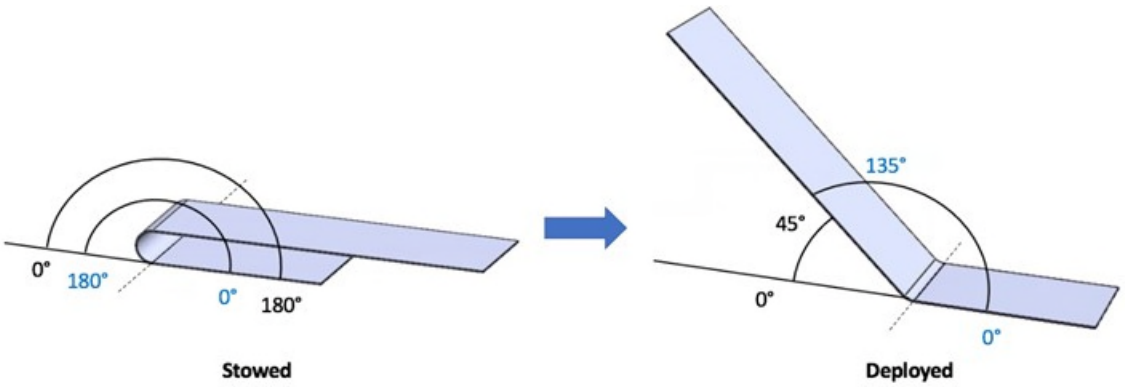

Figure 1. Single nitinol strip deploying to 135 ° representing a non-standard deployment geometry

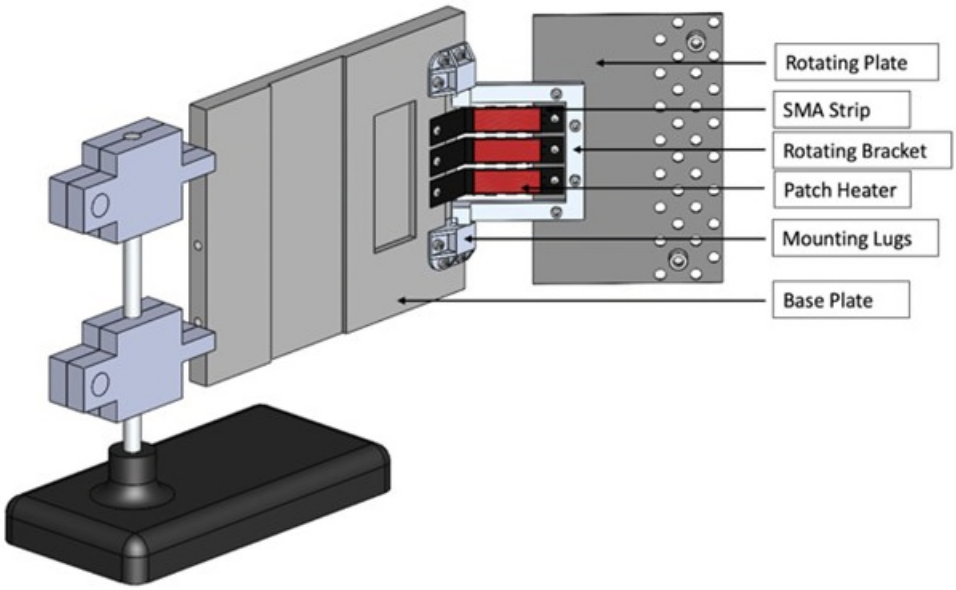

Figure 2. CAD representation of test apparatus

plates, the SMA experienced phase transformation resulting in bracket and plate rotation to the 135° deployment configuration. After full actuation, a locking pin in the mounting lugs secured the rotating hinge to a fixed position. SMA bend line temperature was measured during actuation using LabView and type K thermocouples attached laterally to the bend line via Kapton tape, and hinge rotation angle was measured using MATLAB's image processing toolbox and a downward-facing camera tracking a binary visual target on the top of the rotating plate. This actuation procedure was repeated ten times and compared to predictive model results; test results are not provided because compliance to the model's phase transition predicate, that pre-actuation nitinol phase is fully detwinned martensite without the presence of Rhombohedral phase (R-phase) or glass transition phase, could not be verified. This fully detwinned martensite phase preparation can be accomplished via SMA heat treatment resulting in twinned martensite and subsequent mechanical deformation of the SMA resulting in detwinned martensite at the bend line. While Differential Scanning Calorimetry (DSC) testing of the nitinol samples showed clear martensite-to-austenite phase transition, R-phase and glass transition phases were present. The presence of R-phase did not appear to affect actuation or actuation repeatability, but model verification by test is not assumed to be complete.

SMA Training

The SMA training and heat treatment profile ensures geometry-specific actuation fidelity and repeatability, though imprecise nitinol manufacturing techniques impart inconsistent phase characteristics to nitinol specimens even within the same batch of specimens. The authors observed phase inconsistencies in specimens from a variety of nitinol vendors and nickel contents; it is therefore imperative to DSC test all mechanism-utilized nitinol before heat treatment, after heat treatment, and after detwinning via mechanical deformation to ensure appropriate phases and phase transition temperatures exist for the intended operational environment and to determine martensite-to-austenite transition start, peak, and finish temperatures as inputs to the predictive model. All nitinol considered in the present work was 55.75% nickel by mass procured from Kellogg's Research Labs.

To set the desired actuation shape, a nitinol sheet was constrained in the 135° deployment configuration within an oven or furnace and subjected to high temperatures dependent on the SMA nickel content and actuator geometry. The furnace temperature was then ramped down to adjust the SMA transition temperatures, or the temperatures at which the SMA transitions from detwinned martensite to austenite and vice versa. There exist distinct temperatures for phase transition start, peak transition, and transition finish for each phase transition [4]. Immediately following furnace heat treatment, the sample was subjected to an ice water quench, a high thermal gradient, which causes the martensite-to-austenite transition temperatures and austenite-to-martensite transition temperatures to delineate, reducing phase overlap in the SMA. Once the nitinol has been quenched, it is in a twinned martensite phase that is unpredictable during actuation and easily fatigued, resulting in an actuator lacking repeatability or predictable actuation [11]. Detwinned martensite is an aligned and predictable form of the martensite phase; options for detwinning twinned martensite include manual or mechanical cold work and load frame tensile cycling. Bending the nitinol with any method will achieve partial detwinning, but localized twinned areas may present as opposed to fully detwinned martensite as detwinning occurs at the atomic lattice level. Performing X-Ray Diffraction on a detwinned sample would provide clarity on the level of detwinning after a deformation process. Consecutive tensile cycling, meaning programmed, cyclical loading and unloading on a load frame would be a rigorous, more repeatable detwinning process but requires a load frame and clamps specific to the geometry of the SMA to prevent slipping during tensile cycling operations. For the purposes of preliminary model validation, repetitive rotation of the SMA plates in the test apparatus, nominally 100 rotations, resulted in SMA that displayed slight sporadic behavior during acutation signifying pockets of twinned martensite but did not display actuation fatigue inherent to fully twinned martensite. Again, comparison of model results to test results are not presented here due to the model's phase predicate violation; an example DSC result is provided in Figure 3 characterizing the violation.

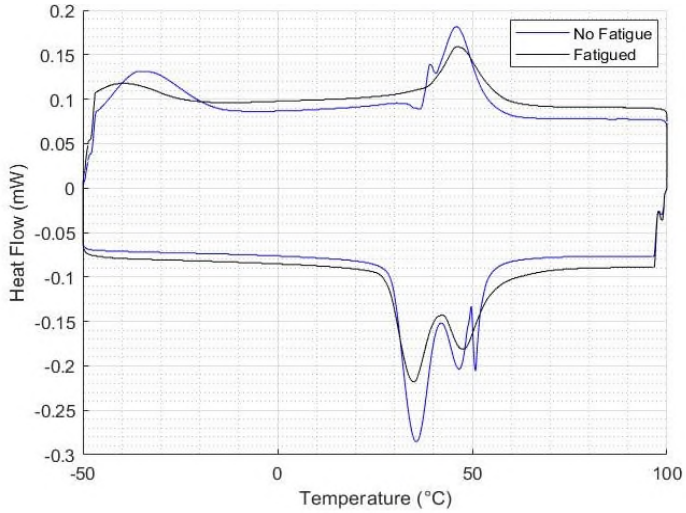

Figure 3. DSC results for a 55.75% nickel SMA sample treated at 550°C for 30 min, ramped down to 400°C at a rate of 5°C/min, and treated at 400°C for 15 min

The SMA in Figure 3 was secured in a mold and placed into a furnace at 550°C for 30 minutes. It was then ramped down to 400°C at a rate of 5°C/min. Once at 400°C, it was aged for 15 minutes. Lastly, both the SMA and mold were quenched in an ice water bath. SMA directly after ice quenching is labeled “No Fatigue”, signifying twinned martensite, and SMA after mechanical work in the test apparatus is labed as “Fatigued”, signifying partial to full martensite detwinning. Instead of smooth, single-peaked transitions from martensite to austenite (heating from bottom left to bottom right) and back (cooling from top right to top left), the phase transitions in this sample contained both R-phase and glass transition phases. The bottom left plateau is martensite, and both the bottom right and top right plateaus are austenite. During the heating phase transition in the non-fatigued martensite, multiple peaks and a “spike” pulse is visible, indicating multiple material phases. Multiple phases are seen in the cooling profile as well. The spike phase and multi-peak transitions smooth out after mechanical work to detwin the martensite, but determination of a clear martensite start, peak, and finish temperature was not possible with this specimen. The top left plateau is at least partially R-phase because another phase transition occurs near -40°C, presumably from R-phase to detwinned martensite. If the test specimen was transitioning from detwinned martensite to austenite upon heating and from austentie to a mix of martensite and R-phase upon cooling, the test could not be considered repeatable, and the predicate of the model is violated. While the model strongly correlates with physical principles and expected actuation behavior, training SMA to transition from only detwinned martensite to austenite at a specific temperature is non-trivial.

Methods exist to remove the spurious phases, though more testing is warranted on purchased specimens with consistent material properties. An increase in the initial furnace temperature leads to a shorter and less pronounced R-phase plateau [12]. In Halvorson et al [10], spike phases were postulated as effects of quenching in liquid nitrogen instead of an ice bath; this has been determined to be incorrect. Multiple DSC test iterations with an ice water quench resulted in spike phases occurring where R-phase is expected near the Austenite finish temperature. The evolution to R-phase to glass phase is poorly documented in literature. It is asserted that the spike phases are glass transition phases; glass phases can occur ranging from 12%-82% nickel by mass [13].

Predictive Actuation Model

The thermal, constitutive, and kinematic behavior of the SMA actuation process was modeled with a MATLAB simulation code divided into three elements: a heat transfer model, a thermo-mechanical model, and a kinematic model. SMA transient thermal response to PH operation in the bending region was determined using a quasi-3D, finite-difference heat transfer model with simulated conduction, convection, and radiation heat transfer effects corresponding to lab and PH input conditions. The thermo-mechanical model employed actuation criteria from Zhou, Yoon, and Leng [14]; the provided temperature distribution at each geometric node and time step was used to determine the transient stress and phase distribution per node. The kinematic model computed a motion-inducing stress relaxation from the thermo-mechanical model at each time step and used this relaxation to determine kinematic parameters such as warm-up time, rise time, and angular velocity. The combination of geometry-specific thermal response, thermo-mechanical stress, and kinematic motion fully characterizes the bending flat plate behavior during phase change.

Thermomechanical Model

The SMA geometric profile was first discretized into an array of rectangular elements called nodes. A single non-linear equation was written for each node using the First Law of Thermodynamics. Each equation was a function of location-specifc heat inflows and outflows present at the node as well as any property variations borne from changes in phase or geometric thickness. Thermal conductivity and specific heat were linearly phase-dependent for SMA and temperature-independent for Kapton, Kevlar, and PH material; radiative emissivity was a function of surface material and was assumed constant with respect to phase and temperature. The average convective heat transfer coefficient for a lab environment was calculated

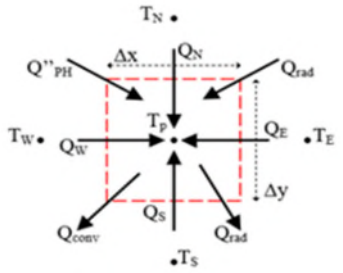

Figure 4. Internal SMA node containing material from patch heater, Kevlar, Kapton, and SMA

using the procedure in Awibi [15], and incident radiation from the walls and lights in a lab environment were modeled using the method outlined by Omori et al. [16]. It is possible to simulate a cold space environment by negating the convective heat transfer coefficient and the input environment radiation, taking the environment temperature to be 2.7 K to represent the Cosmic Microwave Background [17], and adjusting the initial condition to suit a colder space environment. The solution process for deriving the nodal equations begins with an energy balance. The example node in Figure 4 represents an internal node on the rotating section of the SMA flat plate with SMA, Kapton, Kevlar, and PH materials included. The generalized conservation of energy equation is defined in Eq. 1 without internal heat generation.

$$\frac{dE_{sys}}{dt} = \Sigma \dot{E}_{in} - \Sigma \dot{E}_{out} \tag{1}$$

Converting E energy values into Q heat values in Eq. 2, heat inputs were from nodal conduction, a constant heat flux from the PH Q''_{PH}, and radiation $Q''_{rad,in}$ when present. Heat outputs were from convection Q_{conv} and radiation $Q_{rad,out}$.

$$Q_{Transient} = \left[\Sigma Q_{cond,nodal} + \left(Q''_{rad,in} + Q''_{PH}\right) \cdot A\right]_{in} - \left(Q_{conv} + Q_{rad,out}\right)_{out} \tag{2}$$

Nodal areas A were divided into ΔX, ΔY, and ΔZ components representing discretized distances between nodes with only one node in the Z-direction, signifying a quasi-3D model. Conduction terms were replaced with Fourier's Law of Conduction whereas PH and incident radiation heat flux were left as generalized flux terms. The mounted sections of the SMA were assumed to be exposed to convection and radiation heat transfer on one side only. The thermal capacitance of combined Kapton, Kevlar, SMA, and PH material or any combination therein was found using a weighted average by material thickness; SMA specific heat included a term for latent specific energy of phase transformation L_{pc} multiplied by the change of phase per change in temperature $\frac{\partial \xi}{\partial T}$. This term was zero until phase change begins, non-zero during actuation, and zero upon phase change completion; it caused a plateau in the temperature field during phase change as expected. A breakdown of the terms comprising Eq. 2 is shown in Eqs. 3-6; the inputs $Q''_{rad,in}$ and Q''_{PH} were constants. Parameter k represents thermal conductivity, T temperature, ϵ emissivity, σ_{sbc} the Stefan-Boltzmann constant, h convective coefficient, ρ density, c specific heat, z thickness, and t time. Subscripts E, W, N, S represent node directionality with S being the stationary section direction in Figure 2 and N the rotating section direction. Subscript p represents the current node, and i represents the current timestep. The calculation of node-specific thermal conductivity k is geometry-dependent average weighted by thickness and is not provided. Convective coefficient h was constant for the top and bottom.

$$\sum Q_{cond,NB} = \Delta X \cdot \Delta Z \cdot \left(k_N \cdot \frac{T_N - T_{p,i}}{\Delta Y} + k_S \cdot \frac{T_S - T_{p,i}}{\Delta Y}\right) + \Delta Y \cdot \Delta Z \cdot \left(k_E \cdot \frac{T_E - T_{p,i}}{\Delta X} + k_W \cdot \frac{T_W - T_{p,i}}{\Delta X}\right) \tag{3}$$

$$Q_{rad,out} = \Delta X \cdot \Delta Y \cdot \left(\epsilon_{top} + \epsilon_{bottom}\right) \cdot \sigma_{sbc} \cdot \left(T_{p,i}^4 - T_{surr}^4\right) \tag{4}$$

$$Q_{conv} = \Delta X \cdot \Delta Y \cdot \left(h_{top} + h_{bottom}\right) \cdot \left(T_{p,i} - T_\infty\right) \tag{5}$$

$$Q_{Transient} = \Delta X \cdot \Delta Y \cdot \Delta Z \cdot \left[\frac{\rho_{PH} \cdot c_{PH} \cdot z_{PH}}{\Delta Z} + \frac{\rho_K \cdot c_K \cdot z_K}{\Delta Z} + \frac{\rho_{Kevlar} \cdot c_{Kevlar} \cdot 2 \cdot z_{Kevlar}}{\Delta Z} + \rho_{SMA} \cdot \frac{z_{SMA}}{\Delta Z} \cdot \left(c_{SMA} - L_{pc} \cdot \frac{\partial \xi}{\partial T}\right)\right] \cdot \frac{\left(T_{p,i} - T_{p,i-1}\right)}{\Delta t} \tag{6}$$

Eq. 2, when written in the form specified by Eqs. 3-6, is divided by the nodal volume $\Delta X \cdot \Delta Y \cdot \Delta Z$, and $T_{p,i}$ terms are collected on the Left-Hand Side (LHS). The remaining like terms are combined on the Right-Hand Side (RHS) to produce Eq. 7.

$$\left[\frac{C_{total}}{\Delta t}+\frac{k_N+k_S}{(\Delta Y)^2}+\frac{k_E+k_W}{(\Delta X)^2}\right]\cdot T_{p,i}=\frac{k_N\cdot T_N}{(\Delta Y)^2}+\frac{k_S\cdot T_S}{(\Delta Y)^2}+\frac{k_E\cdot T_E}{(\Delta X)^2}+\frac{k_W\cdot T_W}{(\Delta X)^2}+\frac{Q''_{rad}+Q''_{PH}}{\Delta Z}-\frac{(\epsilon_{top}+\epsilon_{bot})\cdot\sigma\cdot\left(T_{p,i}^4-T_{surr}^4\right)}{\Delta Z} \quad (7)$$

$$-\frac{(h_{top}+h_{bot})\cdot(T_{p,i}-T_\infty)}{\Delta Z}+C_{total}\cdot\frac{T_{p,i-1}}{\Delta t}$$

where the effective volumetric thermal capacitance C_{total} is given by,

$$C_{total}=\frac{\rho_{PH}\cdot c_{PH}\cdot z_{PH}}{\Delta Z}+\frac{\rho_K\cdot c_K\cdot z_K}{\Delta Z}+\frac{\rho_{Kevlar}\cdot c_{Kevlar}\cdot 2\cdot z_{Kevlar}}{\Delta Z}+\rho_{SMA}\cdot\frac{z_{SMA}}{\Delta Z}\cdot\left(c_{SMA}-L_{pc}\cdot\frac{\partial\xi}{\partial \mathrm{T}}\right) \quad (8)$$

In preparation for a Tri-Diagonal Matrix Algorithm (TDMA) solution, Eq. 7 may be written as Eq. 9,

$$a_P T_{p,i}=a_N T_N+a_S T_S+a_E T_E+a_W T_W+S \quad (9)$$

Where the coefficients a_N, a_S, a_E and a_W form the off-diagonal coefficients shown in Eq. 10.

$$a_N=\frac{k_N}{(\Delta Y)^2};\ a_S=\frac{k_S}{(\Delta Y)^2};\ a_E=\frac{k_E}{(\Delta X)^2};\ a_W=\frac{k_W}{(\Delta X)^2} \quad (10)$$

It can be shown that the diagonal coefficient a_P is the coefficient of $T_{P,i}$ in Eq. (7). The source term S is comprised of everything that remains after the off-diagonal coefficients are assigned. The nodes adjacent to a rivet were taken to be a Dirichlet constant temperature boundary condition; this was imposed by setting all off-diagonal coefficients at the node to zero, the diagonal coefficient to one, and the source term to the desired temperature. This ensured the solution process will arrive at the boundary temperature. The Neumann constant heat flux boundary conditions were imposed by setting the boundary-side, off-diagonal coefficient to zero and updating the volumetric thermal capacitance term to reflect the reduction in cross-sectional area. Deriving the nodal equations for all nodes yields a large, nearly tri-diagonal set of linear equations suited for a TDMA solution [18]. The inherent non-linearity associated with radiation heat transfer necessitates an iterative approach to ensure the simulation arrives at the correct temperature distribution. Thus, once a solution was obtained from the TDMA, the resulting temperature field was used to re-calculate the source term, and the TDMA was again applied. This process continued until the maximum change in the output temperature field fell below a pre-defined tolerance, ensuring that the resulting temperature field satisfied the heat conduction equation and thus an overall energy balance. Depending on the time step and spatial resolution selected, the system memory requirements of the above heat transfer model can become very large. For this reason, variables defined as a function of both space and time (and initialized as 3D matrices) were written as functions of space alone (2D matrices) and updated each time step. By saving only the needed time steps of these variables, the memory requirements of the heat transfer model were significantly reduced. Any efforts to parallelize the simulation should be focused on the finite-difference TDMA solver as the simulation spends substantial runtime in this section of the predictive model.

Constitutive Model

Three stresses are present in the SMA hinge actuator: stress due to thermal strain σ_{TH} induced by a temperature difference and dependent on the coefficient of thermal expansion α, stress due to pseudoelastic strain σ_{PE}, which is a function of residual strain ε_r and martensite phase fraction ξ, and stress due to mechanical bending σ_{MECH}, which is relaxed during phase transformation. $E(\xi)$ represents the modulus of Elasticity. Thermal and pseudoelastic stress are defined in Eq. 11 and Eq. 12, respectively.

$$\sigma_{TH}=E(\xi)\cdot\alpha\cdot(T-T_o) \quad (11)$$

$$\sigma_{PE}=E(\xi)\cdot\varepsilon_r\cdot\xi \quad (12)$$

Mechanical bending stress has historically been obtained for flat plate geometries by beam theories (such as Euler-Bernoulli beam theory) that typically assume small deflections [19]. Because bending stress calculations that do not violate the small-angle assumption for flat plate geometries are not readily available, mechanical stresses at discrete bending angles were simulated using FEA in Siemens NX. Ten simulations were conducted at angular increments of 15° between the 0° and 135° values depicted in Figure 2 to obtain a mechanical stress distribution that varies with bend angle and martensite phase fraction. For each bend angle, all phase-dependent solid properties were taken to be linear functions of martensite phase fraction,

which was assumed to vary linearly with the hinge bend angle, e.g., an angle of 45° was 33% austenite. The number of bending nodes required to represent the entire bending region is dependent on the material minimum bending radius MBR, the sma thickness z_{sma}, and the lengthwise grid resolution n_y used in the MATLAB heat transfer and kinematic models. This relationship is shown in MATLAB parlance in Eq. 13,

$$n_{bend} = floor\left(\frac{MBR \cdot \pi \cdot n_y}{z_{sma}}\right) + 1 \tag{13}$$

The bending region was divided into twelve nodes to characterize the actuation behavior of the system around the bend line. The "floor" function was employed to ensure the number of bending nodes remained an integer. All discrete bending nodes were evenly distributed above and below the pre-defined center bend line specific to the application geometry. For each finite element simulation, probes were placed at locations corresponding to the y-position of each of the twelve discrete bending nodes; the MATLAB simulation featured the same 12 nodes for the mechanical bending stress distribution and kinematic joints. With this configuration, each of the ten finite element simulations yielded a mechanical stress distribution represented by twelve mechanical stresses in a 10x12 matrix. The deployment angle, which the SMA was trained to deploy to, was considered to be zero mechanical stress at all locations; the maximum stress for a bend line node constrained in the initial U-shape was 806 MPa. Mechanical stresses are provided in the Appendix.

In the MATLAB simulation, the mechanical stress at each set of bend line nodes in the length direction was obtained via linear interpolation of the FEA mechanical stress distribution per the phase fraction found by the heat transfer model and averaged over the bend line. Due to the uneven martensite fraction distribution along the bending region width, the MATLAB simulation will not find a mechanical stress distribution that is identical to one found in the finite element simulation unless the phase fraction distribution is uniform at the bending region. Having obtained values for the mechanical, pseudoelastic, and thermal stresses, the total equivalent stress is calculated for each node using Eq. 14.

$$\sigma_{total} = \sigma_{MECH} + \sigma_{PE} + \sigma_{TH} \tag{14}$$

Using the temperature distribution obtained from the heat transfer model and the stress distribution calculated above, the martensite fraction was determined for each node at each time step. The martensite to austenite transition criteria are found in Eqs. 15-17 using the original nomenclature where A is temperature [14]. The austenite transition start A_s, peak A_p, and finishing temperature A_f were determined by DSC testing. Eqs. 18-20 characterize the transition from detwinned martensite to austenite.

$$\sigma_s^A = (T - A_s) \cdot C_A \tag{15}$$

$$\sigma_p^A = \left(T - A_p\right) \cdot C_A \tag{16}$$

$$\sigma_f^A = \left(T - A_f\right) \cdot C_A \tag{17}$$

$$s_{a1} = \frac{\pi}{2 \cdot \left(\sigma_p^A - \sigma_s^A\right)} \tag{18}$$

$$s_{a2} = \frac{\pi}{2 \cdot \left(\sigma_f^A - \sigma_p^A\right)} \tag{19}$$

$$\xi_s = \begin{cases} \xi_{s0} \cdot \left\{\frac{s_{a2}}{s_{a1}+s_{a2}} \cdot \cos[s_{a1} \cdot (\sigma_{tot} - \sigma_s^A)] + \frac{s_{a1}}{s_{a1}+s_{a2}}\right\} & for\ \sigma_p^A \le \sigma_{tot} \le \sigma_s^A \\ \xi_{s0} \cdot \left\{-\frac{s_{a1}}{s_{a1}+s_{a2}} \cdot \sin\left[s_{a2} \cdot \left(\sigma_{tot} - \sigma_p^A\right)\right] + \frac{s_{a1}}{s_{a1}+s_{a2}}\right\} & for\ \sigma_f^A \le \sigma_{tot} \le \sigma_p^A \end{cases} \tag{20}$$

Kinematic Model

The equation of motion describing the actuation dynamics of a flat plate SMA geometry is defined in Eq. 21 as a function of mass moment of inertia I_{tot}, stiffness coefficient K, and kinematic torque τ_{bend}. The motion of the system is independent of the angular velocity at each bending node. While the gravitational body force was neglected in the kinematic formulation due to the orientation of the testing apparatus, it could be

incorporated in the kinematic model by adding the cross product of the gravitational force vector and the vector extending from the bending region to the system center of mass to the equation RHS. The stiffness and torque change in response to a change in martensite fraction; this produces a smooth actuation without the oscillation pattern that is normally expected from an Ordinary Differential Equation (ODE) of this form.

$$I_{tot} \cdot \ddot{\theta} + K \cdot \Delta\theta = \tau_{bend} \tag{21}$$

The coefficient I_{tot} represents the mass moment of inertia of the rotating portion of the system and was obtained via the parallel-axis theorem to calculate the inertia of each system component about the rotation axis. The system response time is a strong function of inertia; care should be taken to ensure it is calculated accurately. The stiffness coefficient K is calculated by Eq. 22, where $E(\xi)$ is Young's Modulus as a function of martensite fraction averaged across the bend line, J is the area moment of inertia of the SMA cross-section, and L_{bend} is the length from the center of the bending region to the top edge of the SMA [20]. The $\Delta\theta$ in the stiffness term represents the angular deflection of the bending node from its standard equilibrium point, which was taken to be the angle state at the previous time step to prevent the stiffness term from being non-zero when the torque is zero.

$$K = \frac{E(\xi) \cdot J}{L_{bend}} \tag{22}$$

The input torque τ_{bend} drives the motion of the system and is calculated by Eq. 23. The parameters A_C and z_{SMA} represent the SMA cross-sectional area and thickness, respectively.

$$\tau_{bend} = \sigma_{PH} \cdot A_c \cdot z_{SMA} \tag{23}$$

The phase relaxation stress σ_{PH} can be calculated using one of two variations; without formal model verification by test it is unclear which is correct. Eq. 24 characterizes the relaxation stress as a function of both mechanical (bending) stress and pseudoelastic stress, while Eq. 25 shows the relaxation stress as a function of mechanical stress alone. Either approach could be valid and the distinction between the two is a major point of investigation. The desired relaxation stress behavior (zero→non-zero→zero) occurs regardless of the form of the relaxation stress. Thermal stress was neglected in the calculation of the relaxation stress due to its small magnitude relative to the other stress modes present in the system.

$$\sigma_{PH} = \frac{d\sigma_{MECH}}{dt} \cdot \Delta t + \frac{d\sigma_{PE}}{dt} \cdot \Delta t \tag{24}$$

$$\sigma_{PH} = \frac{d\sigma_{MECH}}{dt} \cdot \Delta t \tag{25}$$

At each time step, all phase-dependent properties and stresses were averaged across each discrete bending node. Eq. 21 was then evaluated at each bending node using the implicit Backward Euler method to determine the angle state and angular velocity for the time step. The Backward Euler method was selected for this application due to its lack of reliance on the previous angle state, which is needed to model the stiffness term in Eq. 21 accurately. An effect of the form of the ODE shown in Eq. 21 is that the system will not halt motion once phase change has completed. It is necessary to set individual angular displacements and angular velocities to zero once they reach the trained angle state.

Predictive Actuation Results and Model Sensitivity

The parameters employed for the reference case study are summarized in the Appendix. The predictive model was run with varied inputs against a reference case; the results were compared to the reference study to determine the sensitivity of the system to the input parameters. Additionally, the model was run with and without the influence of pseudoelastic stress in the torque calculation and in the phase fraction comparison to determine the effect of these parameters on the actuation dynamics of the system. The results of the sensitivity study indicate that the patch heater power, critical stress constant C_A, mass moment of inertia, and the maximum residual strain have the greatest impact on the dynamic response of the system. A change in any of these variables yielded a comparatively large change in the warm-up time and rise times of the system. Tables 1-4 show the influence of these variables in determining the system rise times. All other parameters adhere to reference case parameters provided in the Appendix.

Table 1. Effect of patch heater power on system rise times

Patch Heater Power, [% of Total]	Warm-Up Time, [s]	10% Rise Time, [s]	90% Rise Time, [s]
75%	40	60	90
100%	27	46	66
150%	15	33	51
200%	11	28	45

Table 2. Effect of critical stress constant on system rise times

C_A, [MPa/K]	Warm-Up Time, [s]	10% Rise Time, [s]	90% Rise Time, [s]
9.85	Did not actuate – required temperature too high		
35	27	35	27
50	23	50	23
100	19	100	19

Table 3. Effect of mass moment of inertia on system rise times

Mass Moment of Inertia, [kg-m^2]	Warm-Up Time, [s]	10% Rise Time, [s]	90% Rise Time, [s]
4.72·10-4	27	31	50
5.60·10-4	27	31	50
6.64·10-4	27	46	66
6.96·10-4	27	93	145

Table 4. Effect of residual strain on system rise times

Residual Strain, [%]	Warm-Up Time, [s]	10% Rise Time, [s]	90% Rise Time, [s]
1.0%	27	46	66
3.0%	37	54	77
5.0%	49	66	94
6.7%	Did not actuate – required temperature too high		

Table 5 shows the effect of residual stress on the actuation behavior of the system. The increase in equivalent stress brought on by residual stress allows the relaxation stress induced by phase change to be much larger. Thus, systems including residual stress tend to actuate faster than those without .

Table 5. Effect of pseudoelastic stress inclusion to relaxation stress on system rise times

	Warm-Up Time, [s]	10% Rise Time, [s]	90% Rise Time, [s]
Pseudoelastic Stress	28.0	46.0	66.0
No Pseudoelastic Stress	28.0	59.0	88.5

Figure 5 shows the temperature and martensite fraction contours at 45 seconds and after the system has reached steady state. It is clear the thermal behavior of the hinge does not limit the size of the bending region in any way, as the system achieves the required actuation in the entire bend line at steady state. It can be observed from the martensite fraction contours in Figure 5 that phase change at the bending region does not occur uniformly but from the outside in; the stress required to achieve phase change is larger in the center of the bending region than in the sides. Since the center of the bending region has a higher "critical stress" σ_{tot} than the rest of the bending region, it requires a higher temperature to actuate; nodes do not actuate in order of proximity to the patch heater.

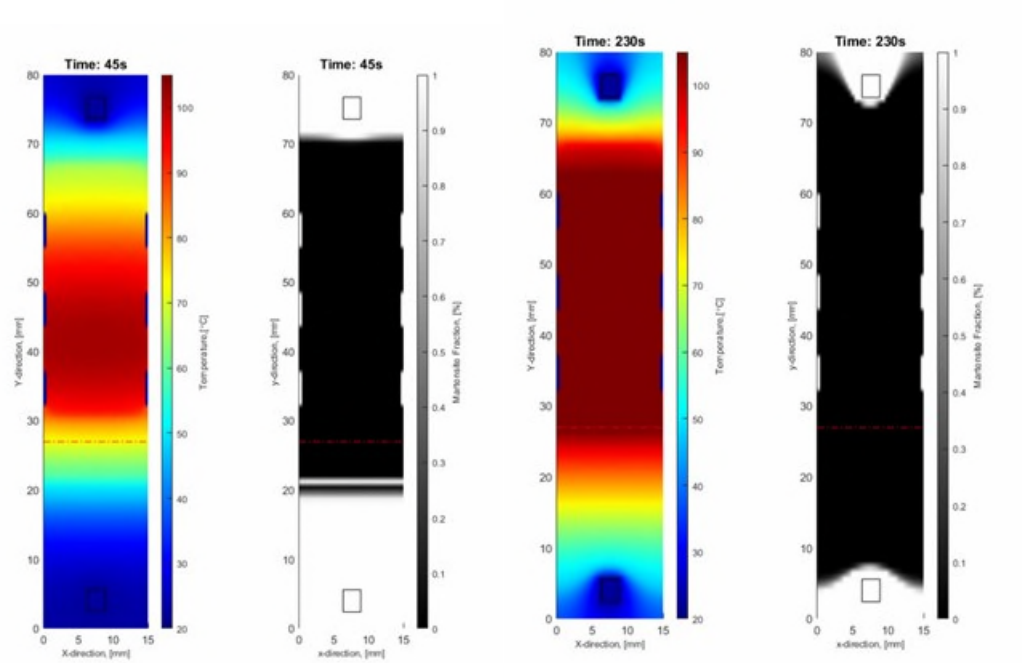

Figure 5. (left) Temperature and phase distributions at 45 s actuation time, (right) Temperature and phase distributions at steady state. The central bend line is shown dotted in red.

Figure 6 shows the kinematic behavior of each discrete bending node as well as the composite bend angle. Each bending node exhibits roughly uniform behavior, but actuation order is dependent on nodal σ_{tot}. This results in a system actuation profile where behavior near the trained deployment angle is greatly dependent on the stress distribution of the hinge. A maximum stress at a node that is much greater than stresses of neighboring nodes will result in additional time needed for bending actuation. This behavior can be mitigated with an increase in the critical stress constant C_A or a decrease in maximum residual stress.

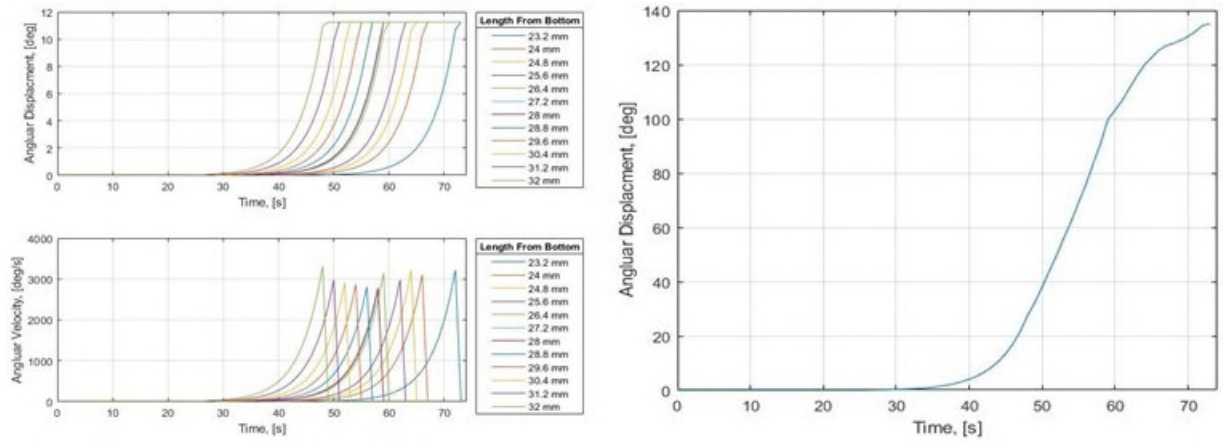

Figure 6: Discrete bend angles (top left), discrete angular velocities (bottom left), and total bend angle (right) vs. time

As is true of all material phase changes, thermal energy can be converted into phase change energy if energy requirements are met. Figure 7 depicts the full actuation of the system until the hinge geometry reached steady state. Evident is the temperature plateau indicating phase change energy conversion.

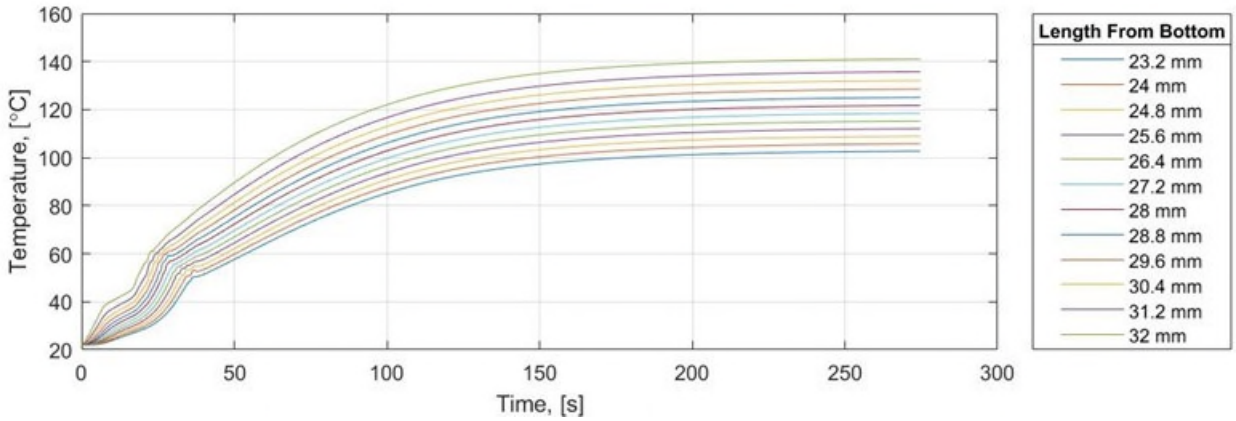

Figure 7: Temperature per node as a function of time until steady-state is reached

Conclusions

The actuation of flat plate SMA that is shape trained into a non-standard deployment geometry, heat treated to twinned martensite phase, and mechanically worked to detwinned martensite phase can be modeled using thermomechanical, constitutive, and kinematic relations yielding valuable mechanism considerations such as rise time. While the shape training aspect of heat treatment is achieved simply by constraining the plate in the intended deployment geometry using a mold, any thermal recipe to convert untrained SMA into detwinned martensite SMA must be specific to both the SMA manufacturing process and pre-treatment DSC results due to the presence of material phases other than martensite and austenite. Model verification by test was performed for the considered model, but the model predicate of phase transition from solely detwinned martensite to austenite could not be verified by DSC test in the SMA actuation test specimens due to the persistent presence of R-phase and glass transition phases. Test results, while informally in good agreement with model results, were therefore not included in this work for comparison to predictive model results; the model is considered unverified and unvalidated yet scientifically rigorous.

Residual stress is included in the equivalent stress actuation criteria via the pseudoelastic stress term, but it is unclear if torque-inducing relaxation stress should be a function of pseudoelastic stress without formal verification by test. Including residual stress in the stress relaxation term decreases actuation rise time because the hinge torque increases. However, if too much residual stress exists in the SMA after heat treatment, the system will not actuate because the critical stress criteria is not met to initiate actuation even if the SMA is above its actuation temperatures. Rise times are also heavily dependent on critical stress constant, which is a change in internal unit stress per change in unit temperature and has wide disparity in reported values. Critical stress constant determination may vary per SMA manufacturer and may require manufacturer input.

Prediction of kinematic parameters such as rise time was enabled by high-fidelity thermal modeling using geometry-specific nodal energy balances and TDMA solution methodologies. While nodal temperatures increased over time with controlled heat input from the mounted patch heater and expectedly plateaued as phase change occurred at each node, an unexpected yet legitimate discovery was that the plate changed phase from the outside-in on the non-rotating section of the SMA due to mechanical bending stresses present at that near-bend line location. Away from the bend line, the SMA actuated as the nodal temperature exceeded the actuation temperature. Near the bend line, the mechanical stresses prevented actuation until the nodal temperature exceeded the actuation temperature inversely proportionate to the value of the critical stress constant. If the critical stress constant is low, the bend line temperatures must greatly exceed actuation temperatures for the system to actuate, sometimes unrealistically so. If this scenario is unavoidable in a given geometry, it is possible to accommodate for a low critical stress constant by heat treating the SMA during shape training to lower actuation temperatures.

Acknowledgements

The authors would like to thank the Alabama Space Grant Consortium for its continued support in all aspects of workforce development in the commercial space sector. Dr. L. Dale Thomas is thanked for his direction and leadership of the consortium and the Complex Systems Integration Lab at the University of Alabama in Huntsville. Dr. David Beale is thanked for championing shape memory alloy research in the state of Alabama.

References

[1] Eschen, K., Granberry, R., & Abel, J. (2020). Guidelines on the design, characterization, and operation of shape memory alloy knitted actuators. Smart Materials and Structures, 29(3), 035036.

[2] Reynaerts, D., & Brussel, H. V. (1997, December 22). Design aspects of shape memory actuators. Mechatronics, 8(6), 635-656. doi:10.1016/s0957-4158(98)00023-3

[3] Mohd Jani, J., Leary, M., & Subic, A. (2017). Designing shape memory alloy linear actuators: A review. Journal of Intelligent Material Systems and Structures, 28(13), 1699-1718.

[4] Zhou, B., Liu, Y., & Leng, J. (2010). A macro-mechanical constitutive model for shape memory polymer. Science China Physics, Mechanics and Astronomy, 53 (12), 2266-2273. doi:10.1007/s11433-010-4163-2

[5] Jayender, J., Patel, R., Nikumb, S., & Ostojic, M. (2008). Modeling and Control of Shape Memory Alloy Actuators. IEEE Transactions on Control Systems Technology, 16(2), 279-287. doi:10.1109/tcst.2007.903391

[6] Brinson, L. (1993, April). One-Dimensional Constitutive Behavior of Shape Memory Alloys: Thermomechanical Derivation with Non-Constant Material Functions and Redefined Martensite Internal Variable. Journal of Intelligent Material Systems and Structures, 4(2), 229-242. doi:10.1177/1045389x9300400213

[7] Stroud, H., & Hartl, D. J. (2020). Shape memory alloy torsional actuators: a review of applications, experimental investigations, modeling, and design. *Smart Materials and Structures*. 5-7

[8] Soother, D. K., Daudpoto, J., & Chowdhry, B. S. (2020). Challenges for practical applications of shape memory alloy actuators. *Materials Research Express*, 7(7), 073001.

[9] Mertmann, M., & Vergani, G. (2008). Design and application of shape memory actuators. *The European Physical Journal Special Topics*, 158(1), 221-230.

[10] Halvorson, Michael c., et al. “A Bending Flat Plate Shape Memory Alloy Model for CubeSat Solar Array Deployment with Thermomechanical, Constitutive, and Kinematic Relations.” *AIAA Scitech 2021 Forum*, 2021, doi:10.2514/6.2021-1792.

[11] Sreekumar, M., et al. “A Compliant Miniature Parallel Manipulator with Shape Memory Alloy Actuators.” *2006 IEEE International Conference on Industrial Technology*, 2006, doi:10.1109/icit.2006.372370.

[12] Duerig, T.W. “Some Unsolved Aspects of Nitinol.” *Materials Science and Engineering: A*, vol. 438-440, 2006, pp. 69–74., doi:10.1016/j.msea.2006.05.072.

[13] Aliaga, L.C.R., et al. “Selection of Good Glass Former Compositions in Ni–Ti System Using a Combination of Topological Instability and Thermodynamic Criteria.” *Journal of Non-Crystalline Solids*, vol. 354, no. 17, 2008, pp. 1932–1935., doi:10.1016/j.jnoncrysol.2007.10.018.

[14] Zhou, Bo, Sung-Ho Yoon, and Jin-Song Leng. "A three-dimensional constitutive model for shape memory alloy." *Smart Materials and Structures* 18.9 (2009): 095016.

[15] Awbi , H. B., “Calculation of convective heat transfer coefficients of room surfaces for natural convection,” Energy and Buildings, vol. 28, 1998, pp. 219–227.

[16] Omori, T., Taniguchi, H., & Kudo, K. (1990). Monte Carlo simulation of indoor radiant environment. International Journal for Numerical Methods in Engineering, 30(4), 615-627. doi:10.1002/nme.1620300405

[17] Fixsen, D. J. (2009). THE TEMPERATURE OF THE COSMIC MICROWAVE BACKGROUND. *The Astrophysical Journal*, *707*(2). https://doi.org/https://doi.org/10.1088/0004-637X/707/2/916

[18] Versteeg, H. K., & Malalasekera, W. (2011). Solution of discretised equations. In *An Introduction to Computational Fluid Dynamics: The Finite Volume Method* (2nd ed., pp. 212–242). essay, Prentice Hall.

[19] Ugural, A. C., & Fenster, S. K. (2020). Bending of Beams. In *Advanced Mechanics of Materials and Applied Elasticity* (6th ed., pp. 242–300). essay, Pearson.

[20] Crews, J. H., & Smith, R. C. (2013). Quantification of parameter and model uncertainty for shape memory alloy bending actuators.*Journal of Intelligent Material Systems and Structures*,25(2), 229-245. doi:10.1177/1045389x13490842

Appendix

Table 6: Mechanical bending stresses at each node along the bend line as a function of node location and coupled bend angle and martensite fraction

ξ_{Def}	σ_M (MPa)	σ_M (MPa)	σ_M (MPa)	σ_M (MPa)	σ_M (MPa)	σ_M (MPa)	σ_M (MPa)	σ_M (MPa)	σ_M (MPa)	σ_M (MPa)	σ_M (MPa)	σ_M (MPa)	Θ (°)
0	0	0	0	0	0	0	0	0	0	0	0	0	45
0.11	39	57	74	82	90	111	116	125	120	117	109	89	60
0.22	55	78	92	118	129	137	158	166	159	150	131	108	75
0.33	86	112	152	188	199	204	207	208	204	196	172	151	90
0.44	102	140	173	197	204	226	238	249	246	237	214	181	105
0.56	199	246	270	301	309	322	330	332	329	321	304	298	120
0.67	208	265	277	311	358	369	374	415	397	380	371	345	135
0.78	239	287	335	368	436	526	574	586	572	567	553	526	150
0.89	281	318	333	382	428	529	574	619	596	578	567	560	165
1	307	319	327	393	426	532	755	806	802	799	796	781	180
Y (mm)	22.29	23.07	23.86	24.64	25.43	26.45	27.00	27.79	28.57	29.36	30.14	32.00	

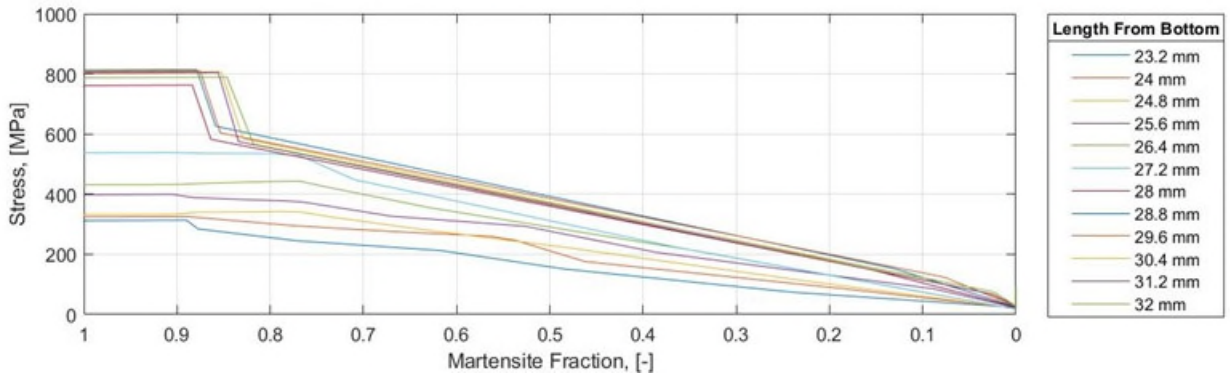

Figure 8: Discrete mechanical bending stresses as a function of martensite fraction

Table 7: Model inputs used as the reference case. Subscript M indicates martensite; subscript A indicates austenite.

Parameter	Value	Unit	Description
n_x	101	node	Number of nodes in the x-direction
n_y	101	node	Number of nodes in the y-direction
ΔX	1.5e-4	m	Nodal dimension in the x-direction
ΔY	8.0e-4	m	Nodal dimension in the y-direction
ΔZ	Variable	m	Nodal dimension in the z-direction
Δt	1	s	Discrete time step
E_M	28	GPa	Elastic modulus of martensitic nitinol
E_A	75	GPa	Elastic modulus of austenitic nitinol
α_M	6.6e-6	1/K	Coefficient of thermal expansion of martensitic nitinol
α_A	11e-6	1/K	Coefficient of thermal expansion of austenitic nitinol
ρ_{SMA}	6,500	kg/m^3	Density of nitinol
ρ_{PH}	2,329	kg/m^3	Density of patch heater
ρ_{kapton}	1,420	kg/m^3	Density of Kapton
ρ_{kevlar}	1,000	kg/m^3	Density of Kevlar
z_{SMA}	0.5e-3	m	Thickness of nitinol
z_{PH}	0.4e-3	m	Thickness of patch heater
z_{kapton}	0.2e-3	m	Thickness of Kapton
z_{kevlar}	0.1e-3	m	Thickness of Kevlar
k_M	8.6	W/m·K	Thermal conductivity of martensitic nitinol
k_A	18	W/m·K	Thermal conductivity of austenitic nitinol
k_{PH}	68.8	W/m·K	Thermal conductivity of patch heater
k_{kapton}	0.12	W/m·K	Thermal conductivity of Kapton
k_{kevlar}	0.04	W/m·K	Thermal conductivity of Kevlar
$C_{p,M}$	451	J/kg·K	Specific heat capacity of martensitic nitinol
$C_{p,A}$	500	J/kg·K	Specific heat capacity of austenitic nitinol
$C_{p,PH}$	710	J/kg·K	Specific heat capacity of patch heater
$C_{p,kapton}$	1,090	J/kg·K	Specific heat capacity of Kapton
$C_{p,kevlar}$	1,420	J/kg·K	Specific heat capacity of Kevlar
$Q''_{rad,in}$	7	W/m^2	Environmental incident radiative heat flux
Q''_{PH}	11,400	W/m^2	Patch heater conductive heat flux
ε_{SMA}	0.2	-	Emissivity of nitinol
ε_{kapton}	0.72		Emissivity of Kapton
h	8	W/m^2·K	Environmental convective coefficient
T_∞	295	K	Ambient temperature
L_{pc}	20,652	J/kg	Latent specific energy for martensite-to-austenite phase change
A_s	318.15	K	Austenite transition start temperature
A_p	320.65	K	Austenite transition peak temperature
A_f	323.15	K	Austenite transition finish temperature
C_A	35	MPa/K	SMA critical stress constant
ε_r	1.0	%	Residual strain
I_{tot}	6.64e-4	Kg·m^2	Mass moment of inertia of the rotating matter
J	1.56e-13	m^4	Area moment of inertia in the SMA cross-section
A_c	7.5e-6	m^2	SMA cross-sectional area
L_{bend}	0.048	m	Length from the center of the bending region to the top edge of the SMA